JOURNAL OF SPACECRAFT AND ROCKETS
Vol. 42, No. 2, March–April 2005

Molecular Dynamics from Remote Observation of CO(*a*) from Space Shuttle Plumes

William L. Dimpfl* and Glenn C. Light†
The Aerospace Corporation, El Segundo, California 90009-2957
and
Lawrence S. Bernstein‡
Spectral Sciences, Inc., Burlington, Massachusetts 01803

Remote satellite observations of plume-atmosphere interaction spectral radiance from 140 to 900 nm have been made of dedicated Space Shuttle Orbiter engine burns above 250-km altitude. The dominant emission feature is the ultraviolet Cameron band system of CO (∼190 to ∼250 nm). It has been observed as a function of the thrust/orbit direction and engine type (orbital maneuvering system or reaction control system). The molecular beam-like characteristics of the plume produce sensitivity in the spatial distributions to chemical reaction product angular distributions and intermolecular potentials that are often gleaned from laboratory molecular beam-type experiments. A new mechanism, including these aspects, has been assigned through agreement of the observed integrated intensity and spatial distribution of radiance with direct simulation Monte Carlo flowfield/chemistry calculations. A minor amount of methane in the exhaust and multiple chemical pathways to CO(*a*), involving reaction with atmospheric atomic oxygen, has been found to explain the observations.

Nomenclature

A	=	unidentified reaction precursor species
A'	=	variable-hard-sphere parameter, Å-(kcal/mole)$^{\omega}$
A''	=	Arrhenius exponential prefactor, cm^3/(deg^n-molecule-s)
a	=	carbon monoxide lowest triplet state letter designation
B	=	unidentified reaction intermediate species or CO(a) product
CO(a)	=	CO($a\ ^3\Pi_r$)
CO($a\ ^3\Pi_r$)	=	electronically excited carbon monoxide in lowest energetic triplet state
E_{act}	=	Arrhenius chemical reaction activation energy, kcal/mole
E_{rel}	=	relative (center of mass frame) collision energy, kcal/mole or eV/molecule
$h\nu$	=	quantum of emitted light, kcal/mole
J	=	molecular rotational quantum number
J_{ss}	=	steady-state CO(a) radiant intensity, W/sr
$J(t)$	=	time-dependent radiant intensity, W/sr
k	=	bimolecular reaction-rate constant, cm^3/(molecule-s)
l	=	exponential potential length parameter, Å
n	=	exponent for inverse r-to-to-the-nth repulsive potential
n'	=	Arrhenius temperature exponent
[O]	=	atomic-oxygen number density, cm^{-3}
R	=	thermodynamic gas constant, 0.001987 kcal/(deg-mole)
r	=	interparticle separation, Å
T	=	absolute temperature, K
T_{rot}	=	nonlocal thermodynamic equilibrium absolute molecular rotational temperature, K
T_{vib}	=	nonlocal thermodynamic equilibrium absolute molecular vibrational temperature, K
t	=	time, s
V_{rel}	=	relative collision velocity, cm/s
v'	=	upper electronic state vibrational quantum number
v''	=	lower (ground) electronic state vibrational quantum number
Γ (arg)	=	gamma function of argument
Δv	=	change in vibrational quantum number
$^3\Pi_r$	=	carbon monoxide a electronic state term symbol
π	=	circle circumference/diameter ratio (3.14159265...)
σ	=	total-hard-sphere cross section, cm^2
τ	=	time constant for reaction, s
ω	=	variable-hard-sphere parameter ($=2/n$)

Introduction

STUDIES of gas-phase chemical reactions have been largely confined to molecular collision energies below 1 eV. This is about the maximum achievable in chemical flames and defines the upper bound for thermal processes. Higher collision energies of small samples are easily achieved through such techniques as the acceleration of ions in electric fields, photodissociation of molecules, or the recoil of molecules from nuclear decay. It is more problematic to produce significant quantities of hyperthermal neutral species to facilitate the laboratory study of their interaction processes at energies above 1 eV, although some progress has been made.[1–3]

The hyperthermal energy regime has become of greater interest since the advent of man-made satellites. Satellites in low-Earth west-to-east orbit traverse the tenuous corotating atmosphere at relative velocities around 7.4 km/s. The thermal velocities of the atmospheric molecules are significant relative to the orbital velocity and are typically around 1 km/s. The energy of collisions between molecules effusing or released from a satellite and the atmospheric species is on the order of 3 eV, well into the hyperthermal regime. It is also of significance that the low-Earth-orbit (LEO) residual atmosphere is predominantly atomic oxygen, a highly reactive species. This results in physical and chemical phenomena associated with

Presented as Paper 2003-6204 at the AIAA Space 2003 Conference, Long Beach, CA, 23–25 September 2003; received 14 January 2004; revision received 6 February 2004; accepted for publication 9 February 2004.

*Senior Research Scientist, M2/251, P.O. Box 92957. Member AIAA.
†Senior Project Engineer, M5/643, P.O. Box 92957.
‡Chief Scientist, 4 Fourth Avenue.

orbiting spacecraft in a regime that is relatively unstudied, poorly understood, and difficult to produce in a laboratory.

Surprisingly, remote observation of light produced by such phenomena in the LEO environment can lead to detailed understanding of fundamental parameters governing them. The length scale and timescales between collisions allow observation of unquenched emission, even from metastable species. Observations by remote satellite-borne (as opposed to in situ) sensors allow spatial and intensity measurements of entire radiant fields that can extend for hundreds of kilometers. These aspects and the well-characterized residual atmosphere allow normally difficult quantitative yield and scattering dynamic determinations to be conducted with relative ease. This study involves the determination of such parameters through the analysis of light produced by the interaction of the exhaust gases from the engines of the Space Shuttle Orbiter with the residual atmosphere. The wealth of information extracted from modeling the emission indicates this technique warrants further development.

The state of knowledge of radiation from plumes has been reviewed recently.[4] The principal radiant energy from the interaction of rocket plumes in LEO with the residual atmosphere comes from infrared emission of collisionally excited major plume gases. The emission analyzed here is found to result from chemiluminescence, involving multiple-step chemistry of a minor plume species with atomic oxygen. Shuttle orbiter plume chemiluminescence has been analyzed previously yielding information about the precursor, mechanism, and kinetics that lead to them[5,6]; and surface glow phenomena on LEO spacecraft have been analyzed yielding mechanistic information.[7] Here, in addition, unprecedented information about the specific dynamics and interaction potentials of the source interactions has been gleaned. Such information is commonly obtained in the laboratory environment from molecular beam-type experiments. In these space experiments there is a similarity in that the exhaust from the orbiter's engines form a directed beam of the exhaust species with a relatively well-defined terminal velocity in the shuttle frame of reference around 3.4 km/s, after expansion into the near vacuum of space. The maneuvering capabilities of the space shuttle allow the exhaust from the various engines to be directed at any angle to the oncoming atmosphere. This allows the relative velocity of the pair-wise collisions between the plume and the atmospheric bath gas to be tuned over a range from 4 to 11 km/s, spanning a collision energy regime of ~3–8 eV.

The analogy with laboratory molecular beam experiments, while useful, is an oversimplification of the space experiment. As in the laboratory, the space experiment samples predominantly bimolecular or single-atom/single-molecule processes. However, unlike the typical laboratory situation, in the space experiment much of the observed radiation can result from species that are the product of multiple collisions/chemical steps. This additional complexity is dealt with by treating the myriad collisions through direct-simulation Monte Carlo (DSMC) techniques.

Observations

Sensors on the Midcourse Space Experiment satellite were used for the observations of this study.[8] The sensors used included UV through near-infrared bandpass and spectrographic imagers, covering from 140 to 900 nm. Detailed information about the sensors has been published elsewhere.[9]

The orbiter's engines include the relatively high-efficiency orbital-maneuvering-system (OMS) engines, with a nominal specific impulse (ISP) of 316 s, used principally for orbit changes and adjustments, and the less efficient reaction-control-system (RCS) engines, with and ISP of 281 s, used principally for attitude control and small orbit changes and adjustments. Both engines burn monomethyl hydrazine propellant and nitrogen tetroxide oxidizer. OMS engines were fired individually, providing 6000 lbf of thrust from a flow of 11.82- and 7.17-lb/s fuel and oxidizer, respectively. RCS engines were fired in aligned pairs, providing a combined thrust of 1680 lbf from a total flow of 4.56- and 2.78-lb/s fuel and oxidizer, 3% richer than the OMS's mixture ratio. Besides the engines' size, their principal difference is the method of cooling the engines combustion chambers. The OMS engine is cooled by a flow of the propellant to the chamber through a jacket surrounding the chamber. The RCS engines are film cooled by 25% of the fuel flow into the chamber being directed along the interior chamber walls.

Table 1 Burn observation viewing parameters

Burn designation	AOA, deg	Range, km	Altitude, km	Aspect, deg	Azimuth, deg
		OMS			
High ram	180	4300	298	46	n/a
Ram	180	4100	268	127	n/a
Perpendicular	91	3900	295	82	117
Wake biased	30	3400	290	123	245
		RCS			
Ram	168	3500	289	59	~0
Perpendicular	97	4100	295	77	117
Wake biased	26	3600	289	116	229

[a] AOA = angle of attack.

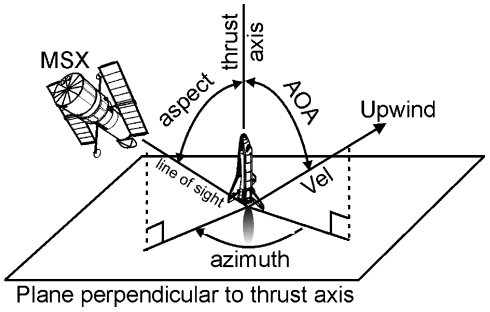

Fig. 1 Burn observation viewing parameter definitions.

The observations reported here include four OMS burns and three RCS burns, made on space transportation system flight 85 (STS-85) (August 1997) and STS-93 (July 1999), at altitudes between 268 and 298 km, where the solar activity, which affects the LEO atmospheric density, composition, and temperature, climbed from minimum to average values. The relevant viewing parameters are defined in Fig. 1 and given for the observations in Table 1. The first two burns were the maneuvers of a Hohmann orbit transfer of STS-85, where the OMS "high ram" burn occurred 2200 km east of Wellington, New Zealand, at a local time of 1:46 a.m., and the OMS "ram" burn occurred over London, England, United Kingdom, at 12:52 p.m. Greenwich Mean Time. The remaining burns were dedicated burns of STS-93, all occurring ~1500 km southeast of Tokyo, Japan, within 10 min of 8:30 p.m. local time. All burns except for the OMS ram burn were performed in the Earth's umbra. Atmospheric definition parameters are given in Table 2. Atmospheric neutral species compositions were determined from the thermospheric model based on mass spectrometer and incoherent scatter data (MSIS)[10,11] and oxygen ion concentrations were determined from estimated electron densities.[12] All of the burns were performed in neutral species atmospheric compositions that were similar within ±10%, except for the OMS high ram burn, which was conducted at a significantly lower number density.

Spectral Identification and Temporal Development

Among the observed emissions between the 140–900-nm spectral range of the sensors was a prominent and previously unreported emission of the Cameron bands from CO($a\ ^3\Pi_r$) radiating to the ground state, in the 180–300-nm bandpass narrow-field ultraviolet imager (IUN). CO(a) is a metastable state lying 139 kcal/mole (6.03 eV) above the ground state, with an average lifetime of 4.4 ms (Ref. 13). The temporal development of this emission from the OMS High Ram burn is indicated in Fig. 2, where the crosswind image dimension has been integrated to show the developing station radiation along the burn thrust line.

Spectrographic imagers (SPIM), coaligned with the bandpass imagers, indicated the IUN plume radiance was dominated by emission from CO(a). The spectral radiance from the final 20 s of the OMS

Table 2 Burn duration and local atmospheric parameters

Burn designation	Duration, s	Atm. density, $cm^{-3} \times 10^{-8}$	Atm. temperature, K	Atm. mole fraction			
				O	N_2	O_2	O^+
			OMS				
High ram	36.7	2.78	717	0.904	0.093	0.003	0.00030
Ram	36.7	9.43	874	0.727	0.262	0.011	0.00048
Perpendicular	9.6	9.22	1159	0.731	0.258	0.010	0.00010
Wake biased	9.7	9.86	1133	0.727	0.263	0.010	0.00007
			RCS				
Ram	9.5	9.91	1133	0.726	0.263	0.010	0.00007
Perpendicular	9.8	9.24	1154	0.732	0.258	0.010	0.00010
Wake biased	8.0	9.96	1122	0.727	0.263	0.010	0.00007

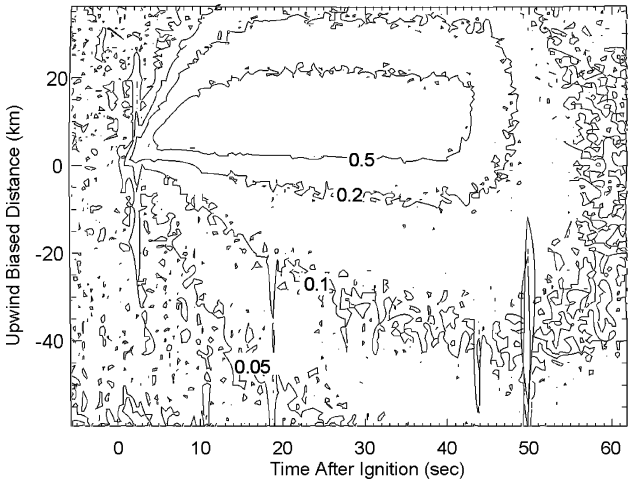

Fig. 2 Developing station radiation from the OMS high ram burn. Black line intensity contours here and in all subsequent figures are on a logarithmic scale with three contours per decade from the peak intensity.

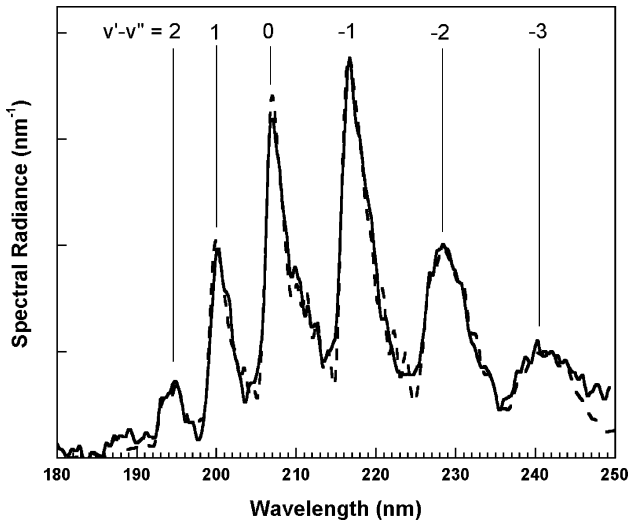

Fig. 3 Spectral features dominating the mid-UV plume radiance, with CO(a) Δv bands identified. Also shown is the model fitted to the data (– – –).

high ram burn from SPIM 2, with a resolution of 0.8 nm, is shown in Fig. 3.

The CO(a) spectrum was fitted (Fig. 3) using a radiative-transfer code that computes the highly excited and nonequilibrium emission from diatomic molecules produced by chemiluminescent reactions.[14] The code utilizes a spectral line compilation (line positions, strengths, and lower state energies) that enables the contribution of each line to be explicitly calculated. The CO(a) spectrum was found to be well described by a nearly Boltzmann distribution of CO(a) vibrational level populations with $T_{vib} = 4500$ K, shown

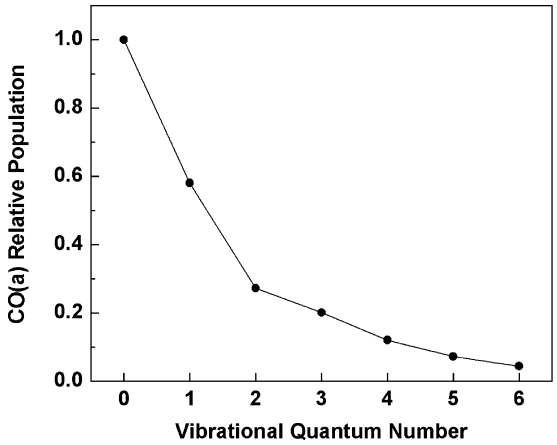

Fig. 4 Vibrational distribution from fit [T = 4500 K with Pop(v' = 2) reduced by 20%].

in Fig. 4. The population of the $v' = 2$ level had to be reduced by a factor of 0.2. However, the rotational distribution, shown in Fig. 5, was found to be more nonthermal. It was initially modeled as a modified Boltzmann distribution in which the rotational population of each level was specified as the product of a Boltzmann factor and an additional weighting factor of J^n, where J is the rotational quantum number of the emitting level. A value of $n = 1$ along with $T_{rot} = 3500$ K was determined from the spectral fit. It was found that a further refinement to the rotational distribution in which the contributions of the lower and higher rotational levels were treated as independent linear combinations resulted in a significantly improved fit. Finally, it was also found that a maximum internal energy cutoff of 1.3 eV had to be imposed on the vibration-rotation energy of the contributing CO(a) emitting levels.

Steady-State Spatial Distribution and Intensity

An image of the steady-state radiance from the final 20 s of the OMS high ram burn, observed in the spectral band from 180–300 nm, is shown in Fig. 6. The total intensity for the region shown is 1940 ± 120 W/sr, corresponding to 1.04×10^{-4} photons per exhaust plume molecule. This is a significant quantum efficiency in energetic photon production from the total plume flow, which is an important constraint, helping to identify the source.

Radiance images of the remaining burns identified in Tables 1 and 2 are shown in Fig. 7, and intensities are shown in Table 3. The images represent the integrated intensity from before ignition to past cutoff. The intensities, reported in Table 3, are based on the actual burn time, assuming the trail off of intensity after cutoff fills in the rise to steady state after ignition.

Analysis

Analysis was performed through seeking agreement between the observed plume Cameron band radiance and DSMC computed predictions of that radiance, simulating the nonreactive and reactive collisions among the plume and atmospheric species.

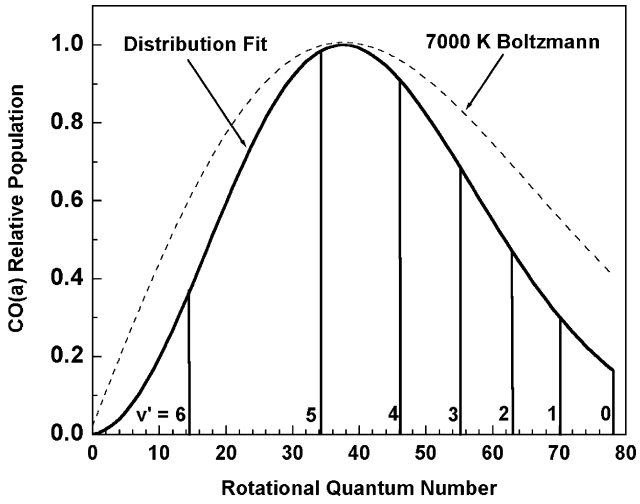

Fig. 5 Rotational distribution from fit. Population cutoff for each vibrational state is shown. Boltzmann distribution with similar peak is also shown.

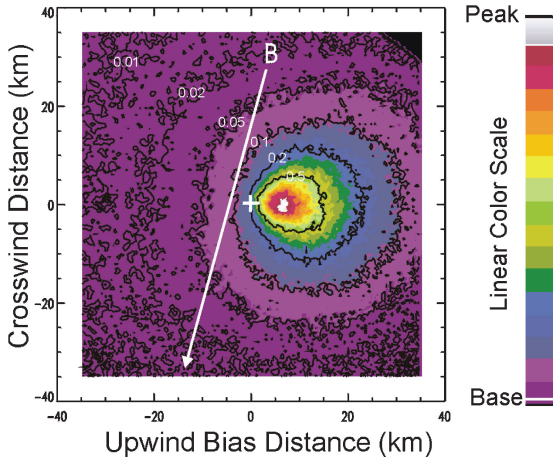

Fig. 6 False color intensity representation of mid-UV radiance from the OMS high ram burn. Shuttle orbiter is located at the cross with plume flowing away and to the right into the oncoming atmosphere. Peak value is 5.2×10^{-10} W/sr-cm^2. The arrow shows the projection of the local Earth's magnetic field.

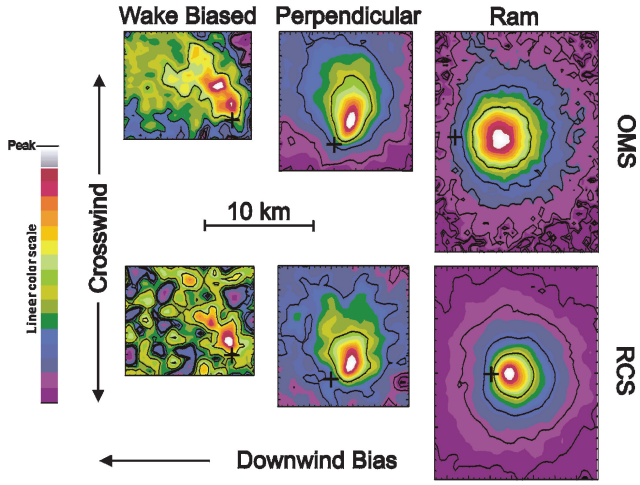

Fig. 7 Radiance images of the remaining burns identified in Tables 1 and 2: +, approximate location of the shuttle orbiter. Intensities are given in Table 3.

Table 3 Steady-state intensities from IUN

Burn designation	Peak radiance, W/sr-cm^2 $\times 10^{-12}$	Integrated intensity, W/sr
	OMS	
Ram	4500 ± 280	2100 ± 130
Perpendicular	430 ± 35	170 ± 14
Wake biased	48 ± 25	19 ± 10
	RCS	
Ram	1200 ± 90	420 ± 32
Perpendicular	230 ± 30	110 ± 13
Wake biased	35 ± 30	12 ± 10

The plume input to the DSMC models comes from the output of an engine computer model: the NASA Lewis two-dimensional kinetics (TDK) engine code.[15] TDK is designed to predict the performance of rocket engines, which is generally not strongly dependent on the mixing of propellants at the injector face. This mixing is not computed by the code, which is generally run assuming perfect mixing of the propellants, yielding an approximate composition of plume gases at the nozzle exit. The one-dimensional kinetics module of the TDK code predicts the following average plume gas mole fraction ratios for both the OMS and RCS engines: $H_2O/N_2/H_2/CO/CO_2/H$::0.32/0.31/0.17/0.12/0.05/0.015, where the mole fraction values predicted are within 10% of these values for either engine type.

The DSMC model used in deciphering the source of the Cameron band radiance was the Spacecraft/Orbiter Contamination Representation Accounting for Transiently Emitted Species (SOCRATES)[16,17] code, which includes bimolecular chemistry. For the axisymmetric cases of the OMS ram burns, a two-dimensional version, the Transitional and Rarefied Axisymmetric Monte Carlo Plume (TRAMP) code, which produces the same result as SOCRATES, but which converges about 10 times faster, was used. Velocity-dependent cross sections for chemical reactions are determined through an inverse Laplace transform of the Arrhenius rate constants, defined by $k = A'' T^{n'} \exp(-E_{\text{act}}/RT)$. {The transform yields the expression $\sigma = \pi^{1/2} A''(1 - E_{\text{act}}/E_{\text{rel}})^{1/2} (E_{\text{rel}} - E_{\text{act}})^{n'} / [2R^{n'} \Gamma(n' + 3/2) V_{\text{rel}}]$.} If n' is positive, this formalism can yield a cross section that exceeds the variable-hard-sphere (VHS) cross section[18] used for computing the total scattering probability. If that occurs, the VHS cross section is used for the reaction cross section.

Ionic Mechanisms

Before attempting DSMC modeling, plausible mechanisms among the known sources of Cameron band emission were sought. Such a mechanism for which the source ingredients are known to be present in the shuttle experiment scenarios is an ionic process. Plume CO_2 will charge exchange with atmospheric O^+ to produce CO_2^+ at the relative energies of the plume-atmosphere collisions.[19] From Cameron band emission seen in the Martian atmosphere, CO_2^+ is known to dissociatively recombine with atmospheric electrons to yield $CO(a)$.[20–22] The spatial distribution of the emission from this process, however, should be strongly influenced by the interaction of the Earth's magnetic field with the ambient O^+ as it is perturbed by the plume. The local magnetic field was inclined 110 deg toward the Earth from the orbiter's atmosphere relative velocity vector and nearly in the vertical plane of the orbit. Its projection on the IUN image plane is shown in Fig. 6. Although the SOCRATES model currently does not include magnetic field effects to accurately predict this process, qualitative examination of Fig. 6 shows potential evidence for a small contribution from it. Subtle horizontal asymmetry in the contours below 10% of the peak radiance is consistent with $CO(a)$ produced by this process through the channeling effect of ions by the Earth's magnetic field.

The secondary importance of this process in the plume observations is also supported by lack of correlation with the large variation

in O^+ density, shown in Table 2, resulting from day/night and altitude differences.

Neutral Mechanisms

It is apparent that processes involving neutral species dominate the source of emission. This is supported also, as will be seen, by similarity in the dimensions of the radiant field predicted by DSMC modeling, using typical hyperthermal collision cross sections ($\sim 10^{-15}$ cm^2) between small neutral exhaust plume molecules and O atoms, the dominant atmospheric species.

Interestingly, kinetic information can be gleaned from following the nonsteady temporal change in the total radiant intensity from Cameron band emission, after both engine ignition and shutdown. The shape of this temporal behavior is an indicator of the number of chemical steps involved in producing the CO(a) emission. If we postulate reactions (1) and (2)

$$A + \mathrm{O} \rightarrow B + \text{other product(s)} \tag{1}$$

$$B + \mathrm{O} \rightarrow \mathrm{CO}(a) + \text{other product(s)} \tag{2}$$

where A is the exhaust plume precursor, O is the atmospheric atomic oxygen, and B is either an intermediate or the radiating species CO(a), the time dependence of the total radiant emission can be derived assuming straightforward kinetics. If CO(a) is produced in a single step, described by product B in reaction (1), and the emission is relatively prompt, the growth in the total emission intensity is given by

$$J(t)_1 = J_{ss}[1 - \exp(-t/\tau_1)] \tag{E1}$$

where τ_1 is a time constant defined by $(\sigma_1 V_{rel}[\mathrm{O}])^{-1}$, where σ_1 is the total-hard-sphere cross section for $A + \mathrm{O}$ collisions at V_{rel}, the relative plume/atmosphere collision velocity ($\sim$11 km/s for ram burns), and [O] is the local atmospheric O-atom number density. For ram burns the VHS total cross section lower limit for τ is about 3.3 s. The inverse exponential functionality of Eq. (E1) rises abruptly after ignition, having and initial linear dependence on time, before asymptotically approaching the steady-state intensity. Conversely, if CO(a) is the product of a second step, described by reaction (2), then the growth of emission intensity is given by

$$J(t)_2 = J_{ss}\{1 - \exp(-t/\tau_2) - \tau_1[\exp(-t/\tau_1) - \exp(-t/\tau_2)]/(\tau_1 - \tau_2)\} \tag{E2}$$

where τ_2 is likewise related to σ_2, the total-hard-sphere cross section for $B + \mathrm{O}$ collisions. This functionality yields an induction behavior after ignition, rising gradually from the baseline and displaying a nonlinear dependence on time right after ignition. Continuing this treatment indicates additional steps also produce an induction behavior but with less sensitivity to information about the individual steps. Figure 8 shows a comparison of the fits of Eq. (E1) and (E2) chosen to match the steepest slope of the changing total plume intensity. Total plume intensity was obtained from integrating the spatial dimension of Fig. 2. Derivation of the shutdown behavior yields identical functionality, but inverted, and has been included in Fig. 8.

The kinetic analysis is an oversimplification, not taking into account the complex mixing of the atmosphere and plume and varying distribution of collision velocities during ignition and shutdown. Still, the salient features of the predicted behavior following ignition and shutdown are believed to be significant, supported by the remarkable agreement with the two-step fit. Furthermore, unpublished DSMC time-dependent modeling has shown the same features. The similarity of the startup and shutdown behavior also indicates the absence of transient phenomena for those events in the observed waveband.

The noticeably better agreement of the two-step fit with the OMS high ram burn is taken to indicate the dominance of multistep processes; consequently, the initial DSMC modeling explored the two-step process of reactions (1) and (2). The spatial radiance distribution was predicted using TRAMP for the conditions of the OMS high ram burn steady-state radiance. A key result from studying this general

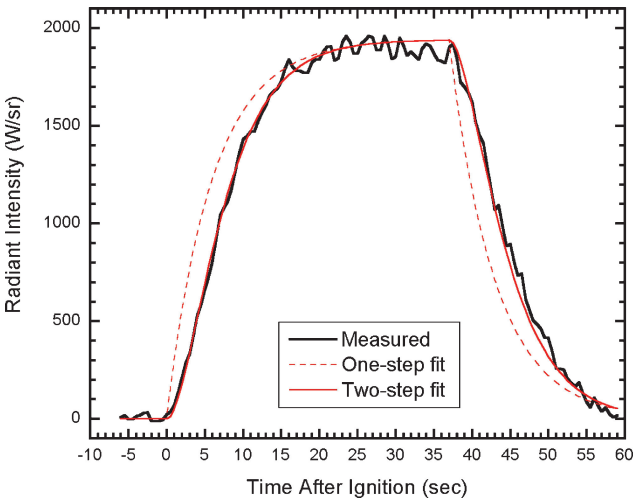

Fig. 8 Comparison of time dependence of total IUN radiant intensity from the OMS high ram burn with that predicted for one-step (τ_1 = 6 s) and two-step (τ_1 = 3.5 s, τ_2 = 4.5 s) processes producing CO(a). Burn shutdown occurs at 36.8 s. The two-step fit is insensitive to interchanging the values of τ_1 and τ_2.

mechanism is that the spatial distribution of the Cameron emission is particularly sensitive to the activation energy of the second chemical step. This is shown in Fig. 9, computed for the scenario of the OMS high ram burn, allowing a definitive fit to the salient shape of the brightest features of the Cameron band radiance.

This shape sensitivity results from the energy required to produce CO(a) in the second step, which imposes a dynamical constraint on intermediate B produced from the first step. For a ram burn, only B intermediates that scatter from reaction (1) with a velocity and a direction similar to that of the precursor A will satisfy the energy requirement to react with an atmospheric O atom to produce CO(a). This constraint biases the radiance to look more like a view of the unperturbed flow of engine exhaust as the activation energy is increased. Based on comparison of the results shown in Fig. 9 with the data shown in Fig. 6, an activation energy of 100 ± 10 kcal/mole (4.33 eV) was found to produce the best fit. It is important to recognize that n', the temperature exponent in the Arrhenius expression, affects the rate at which the cross section increases after the activation energy threshold is reached. This will result in some interdependence between E_{act} and n' and sensitivity to the shape on n', which were not explored.

Precursor Determination

The CO or CO_2 in the plume are obvious candidates for the precursor A in reaction (1) because they are the only plume species identified by the TDK model, which contains carbon. Either of those precursors, however, requires that the intermediate B must be an activated form of CO or CO_2 that is not already in the plume because the principal mechanism is at least a two-step process. Electronically or internally excited states of CO or CO_2 that would live the $\sim$3 s before a subsequent collision with another atmospheric O (the second step) without radiating to the ground state are not known to exist. This leads to seeking minor or trace plume species, not predicted by the TDK engine code run assuming perfect propellant mixing, as candidates for the precursor.

Returning to the plume composition computation, a limitation of the TDK code in predicting engine exit plane compositions is the assumption of perfectly mixed propellants in the engine. The distribution of fuel and oxidizer injection orifices and the inhibited diffusion from the high pressure in the engine chamber contribute to variations in the propellant mixing ratio across the flow of the engine. These variations are known to survive to the engine exit where the exhaust gases expand into space. The term "unmixedness" is often used to describe such oxidizer-to-fuel ratio (O/F) variations (Ref. 4, pp. 14, 15). Additional precursor species that can be produced by these variations can be estimated by computing the engine

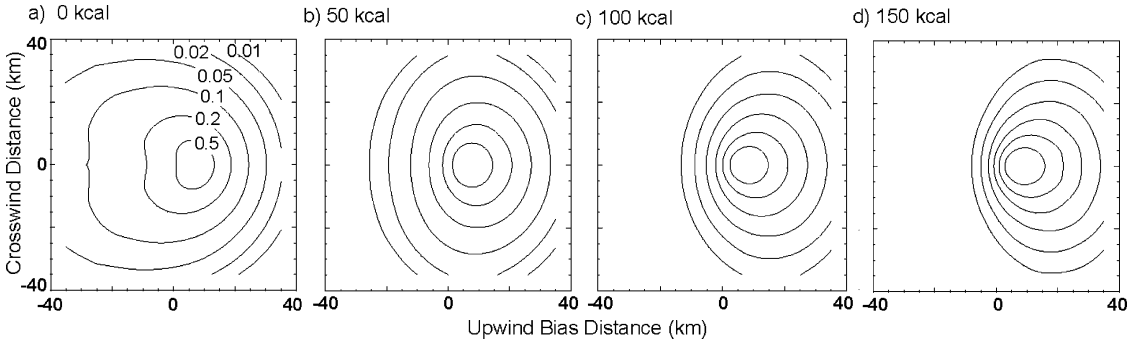

Fig. 9 Sensitivity of the spatial distribution of radiance from two-step process to the activation energy of the second step for the scenario of the OMS high ram burn.

exit equilibrium molecular composition for a range of mixing ratios that might exist in the chamber.

An estimate of O/F distributions in engines is obtained by analysis of visible emission seen in engine tests, such as the air-afterglow emission from NO_2^* produced by $O + NO$ recombination. The high O/F required to explain such emission indicates a very broad O/F distribution with on the order of 1% pure fuel at the fuel-rich extreme. The carbon-bearing species that form in the largest amounts in equilibrium ODK calculations on exit plane compositions for such distributions are CH_4, C_2H_2, and HCN, where the approximate average mole fractions of these species are of order 0.01, 0.001, and 0.001, respectively. The computations yielding these species were performed omitting soot as a possible product, which is justified by its apparent absence in the plumes from OMS and RCS engine tests and the assumption that its formation is limited by kinetic restrictions.

The large O/F variations apparently can exist without large losses in engine efficiency, which results from the average O/F being lower than the stoichiometric ratio for complete combustion to the most stable products. Improved ISP, resulting from regions of higher O/F, help balance losses in ISP from regions of lower O/F.

Among the predicted minor species, C_2H_2 (acetylene) appears promising. It has a high heat of formation, offering energy for the formation of CO(a), and is known to react with atomic oxygen at room temperature to produce Cameron band emission.[23] However, the mechanism found for that emission cannot be a significant process in the plume observations, because the visible emission from the higher d, e, and a' states that are known to populate CO(a) by this mechanism are not seen, and a high activation energy is not involved in their production. The numerous known branches for the $O + C_2H_2$ reaction producing dark products also limit the ability to achieve the observed CO(a) intensity by siphoning the efficiency into the other channels.

Although more CH_4 (methane) than acetylene is predicted in the plume, it initially seemed a less likely precursor because it is a much more stable molecule. Only one first-step reaction of O atoms with CH_4 was known at the time of this analysis,[24]

$$CH_4 + O \rightarrow CH_3 + OH \tag{1a}$$

and that proceeds very slowly at room temperature with an Arrhenius activation energy of 7.2 kcal/mole (0.31 eV). [Subsequent to the analysis the existence of a channel producing $H + OCH_3$, which becomes significant above 2.5-eV relative collision energy, was discovered.[3,25,26] The addition of this channel will affect the efficiency of producing CO(a) from CH_4, but not significantly enough to affect the plausibility of the postulated mechanism. Kinematic constraints restrict the possibility of this new channel from being a principal pathway to CO(a). The OCH_3 product is constrained to have a velocity close to the center of mass of the reactant pair, significantly reducing its ability to overcome the energy barrier for forming CO(a) or reproducing the observed spatial distribution.] However at the plume/atmosphere collision velocities in LEO, this activation energy is easily overcome and implies nearly quantitative conversion of the precursor to the intermediate CH_3 if other reaction branches are insignificant. This points to CH_3 (methyl radical) as a potential intermediate that could produce CO(a).

There is strong evidence for at least two channels to the $CH_3 + O$ reaction, one producing CO and the other producing comparable amounts of H_2CO (formaldehyde).[27] This supports the feasibility of the necessary reaction for the second step:

$$CH_3 + O \rightarrow CO(a) + H + H_2 \tag{2a}$$

Although this reaction, producing electronically excited CO, has not been identified previously, it easily meets the energy conservation constraints, does not violate spin conservation rules, and is endothermic by 69.7 kcal/mole (3.02 eV). This is comfortably below the 100 kcal/mole activation energy required for the second step and leaves up to 50 kcal/mole (2.2 eV) to be distributed among the degrees of freedom of the products, where CO(a) was found to have up to 30 kcal/mole (1.3 eV) of internal energy through the spectral fitting. The high activation energy required for this second step and the difficulty of observing the emission from metastable CO(a) in the laboratory are consistent with this reaction not already having been identified.

Chemical Dynamics Insight

The 100-kcal/mole activation energy found for reaction (2) imposes an efficiency constraint on producing the observed radiance from CH_4. This constraint has led to an important insight to a necessary upgrade to the DSMC codes. A minimum relative collision velocity of 10.4 km/s for producing CO(a) from $O + CH_3$ is required to overcome the 100-kcal/mole energy barrier. Somehow, in the OMS high ram burn scenario the velocity of the CH_4 exiting the engine nozzle must be efficiently imparted to the CH_3 product of reaction (1a) for efficient production of CO(a). In fact, such chemical dynamics are well known and favored at high relative collision velocities. The process where an oxygen atom "snatches" a hydrogen atom from CH_4, leaving it largely unchanged in its direction of motion, is referred to as the "spectator-stripping" mechanism.[28]

DSMC codes typically treat the scattering from both nonreactive and reactive collisions as isotropic. While reactive scattering can have distinct directionality, subsequent collisions rapidly dull the memory of the preferred direction, rendering isotropic scattering a useful approximation for many problems. In our case however, the directionality is critical to the efficiency of reaction (2).

DSMC model computations including idealized spectator stripping dynamics for reaction (1a) were performed, yielding additional support for its inclusion. Figure 10 shows the spatial improvement in the agreement with the OMS high ram burn by changing the product scattering distribution from isotropic to perfectly forward peaked. The intensity contours are stretched in the upwind direction relative to isotropic scattering, yielding a better match with the observed contours of the highest intensity. Incorporating spectator stripping also yields the expected enhancement in the chemical yield by a factor of 2.2 and a reasonable agreement with the observed peak radiance.

Additional CO(*a*) Contributions

The comparison of the data and model radiance contours in Fig. 10 shows growing differences in their relative shape below 10% of the peak value. A contribution with a stronger downwind bias than the two-step process is apparent. The distribution of the residual radiance is consistent with the broader spatial extent of radiance resulting from a three-step process. Subtle differences in the Cameron band spectrum between the peak radiance region and the downwind region (vibrationally hotter), also support the presence of multiple processes.

Again, efficiency constraints enable extraction of significant information from the individual processes contributing to this three-step chain of events. The residual intensity in the field of Fig. 10, after subtracting the intensity from the two-step process, scaled to fit the peak radiance, is 28% of the total radiance. The high chemical efficiency from a process with so many steps points again to CH_4 as the probable source, with reaction (1a) as the first step:

$$CH_4 + O \rightarrow CH_3 + OH \quad (1a)$$

$$CH_3 + O \rightarrow \text{ 2nd intermediate + other product(s)} \quad (3)$$

$$\text{2nd intermediate} + O \rightarrow CO(a) + \text{other product(s)} \quad (4)$$

The spatial distribution of the residual radiance indicates that reaction (4) does not have a significant activation energy (<15 kcal/mole). The sensitivity of the total intensity to angle of attack (shown in Table 3), however, indicated an activation energy of ~50 kcal/mole (2.2 eV) in one of the steps, which then must reside in reaction (3). These constraints leave only CH_2, CH, and CHOH as possible candidates for the second intermediate. Further DSMC analysis was insensitive to the choice among these, and CH_2 was chosen as the most probable second intermediate for the final modeling studies:

$$CH_3 + O \rightarrow CH_2 + OH \quad (3a)$$

$$CH_2 + O \rightarrow CO(a) + H_2 \quad (4a)$$

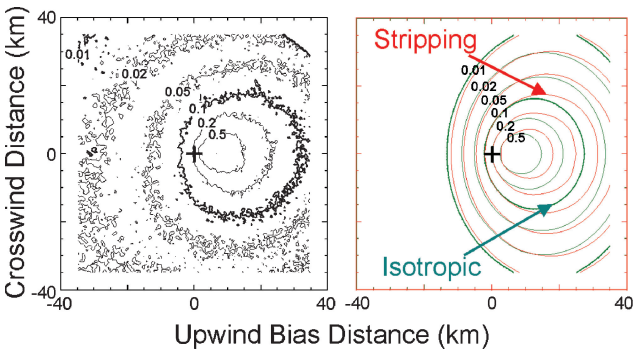

Fig. 10 Improvement in the fit to the radiance distribution by including spectator-stripping dynamics for reaction (1a).

Full Reaction Set Modeling

Table 4, which indicates the chemistry used in the DSMC calculations, shows reaction enthalpies, rate constant parameters, and resulting cross sections at relevant energies, including the Arrhenius prefactors selected for the postulated chemistry of reactions (2a), (3a), and (4a). Besides the two- and three-step mechanisms, the reaction set includes CO(*a*) quenching and chemistry from the National Institute of Standards and Technology database,[29] that could potentially affect the outcome by depleting reactants.

A mole fraction of 0.01 CH_4 was added to the exit plane exhaust composition. Computations were performed so that the production of CO(*a*) by reactions (2a) and (4a) could be followed separately. The relative contributions of the two- and three-step radiance distributions were adjusted, along with the absolute scale, to obtain the best fit to the OMS high ram burn, as shown in Fig. 11. The contribution from the three-step process was reduced to 60% of that computed to obtain the fit shown.

Molecular Potential Insight

Although the fit of the shape of the contours in Fig. 11 is relatively good, the spatial extent of the computed plume is too small by a factor of 1.4, indicating that the mean free path in the model was too small. A similar discrepancy was found for the other ram burns as well, indicating that it was unlikely that the difference was caused by an error in the atmospheric number density, which is generally modeled within a 15% at these altitudes, using MSIS. The other parameter on which the mean free path is dependent is the total collision cross section. That the total collision cross sections in the model are too large was already indicated in the fit of Eq. (E2) in Fig. 8. The total cross sections derived from the time constants of the fit are slightly smaller than those used in the model.

The variable-hard-sphere (VHS) model implements the repulsive interaction potential in the DSMC computations used here.[17] The term "hard sphere" refers to the hard sphere-like isotropic scattering

Table 4 DSMC reaction enthalpies, Arrhenius parameters, and sample cross sections

No.	Reaction	Enthalpy,[d] kcal/mole	Arrhenius parameters			Sample cross sections, $cm^2 \times 10^{16}$, E_{rel}, eV		
			A''	n'	E_{act}	5	8	11
	Methane to CO(a) chemistry							
1a[a]	$CH_4 + O \rightarrow CH_3 + OH$	2.4	1.75×10^{-15}	1.5	8.66	8.35	11.5[c]	9.82[c]
2a	$CH_3 + O \rightarrow CO(a) + H + H_2$	69.7	2.0×10^{-10}	0	100	0	0	0.593
3a[a]	$CH_3 + O \rightarrow CH_2 + OH$	7.0	1.0×10^{-10}	0	50	0	0.492	0.676
4a	$CH_2 + O \rightarrow CO(a) + H_2$	−39.5	1.0×10^{-10}	0	0	2.00	1.25	0.909
5	$CO(a) + M \rightarrow CO + M$	−130.5	1.0×10^{-10}	0	0	2.00	1.25	0.909
6	$CO(a) \rightarrow CO + h\nu$	−138.5	7.04×10^{-3} s[b]	——	——	——	——	——
	Reactant depletion chemistry							
7	$CH_3 + O \rightarrow CO + H + H_2$	−68.8	6.27×10^{-11}	0	0	1.25	0.784	0.570
8	$CH_3 + O \rightarrow CH_2O + H$	−68.4	8.4×10^{-11}	0	0	1.68	1.05	0.764
9	$CH_3 + H \rightarrow CH_2 + H_2$	5.2	1.0×10^{-10}	0	15.0	0	0	0
10	$CH_2 + O \rightarrow CH + OH$	−0.2	1.0×10^{-10}	0	0	2.00	1.25	0.909
11	$CH_2 + O_2 \rightarrow CO_2 + H_2$	−186.1	3.0×10^{-10}	0	0.79	5.92	3.73	2.72
12	$H_2O + O \rightarrow OH + OH$	17.0	7.59×10^{-15}	1.3	17.1	2.30	13.4[c]	11.4[c]
13	$OH + O \rightarrow O_2 + H$	−17.0	7.48×10^{-10}	−0.5	0.06	0.119	0.047	0.025
14	$N_2 + O \rightarrow NO + N$	75.0	3.0×10^{-10}	0	76.7	0	0.452	1.89
15	$CO_2 + O \rightarrow O_2 + CO$	8.1	2.82×10^{-11}	0	52.8	0	0.226	0.213

[a]These reactions were programmed to produce spectator stripping product scattering.
[b]Rate entered as a radiative lifetime.
[c]Cross section limited by VHS total cross-section value.
[d]Reaction enthalpies computed from standard heats of formation at 298 K.

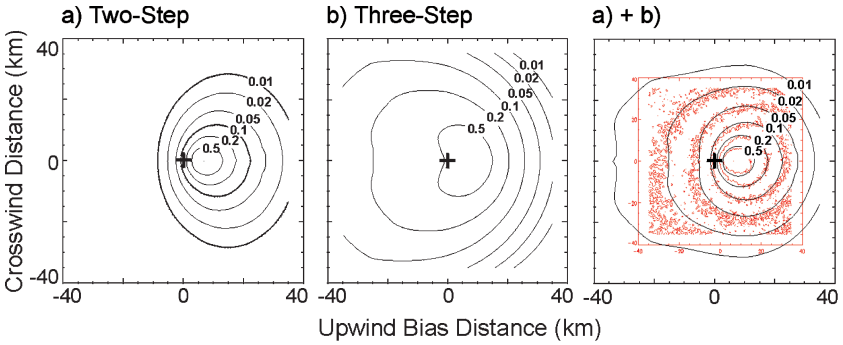

Fig. 11 Combination of two- and three-step processes to fit the observed radiance. The mapped radiant intensity from the three-step process is 30% of the total mapped radiance.

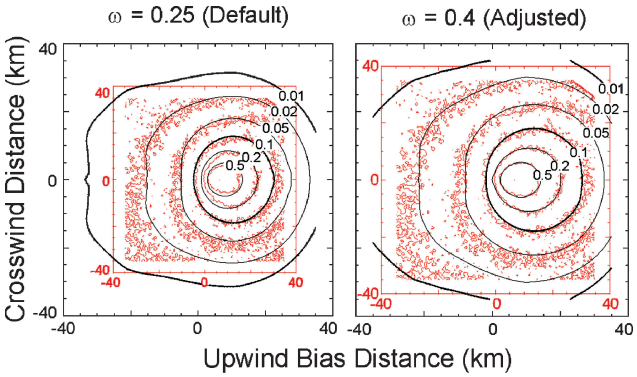

Fig. 12 Improved fit to OMS high ram burn obtained from adjusting VHS ω parameter.

distribution that is used. The term "variable" refers to the fact that the size of the hard-sphere molecules and atoms is adjusted, based on the relative energy of the collision in question. The model is based on an inverse r-to-the-nth repulsive potential formalism, where r is the interparticle separation and n is an integer chosen to represent the stiffness of the repulsion. It is described by the formula $\sigma = A' E^{\omega}$, where σ is the area of the circle with a radius of the distance between particle centers when the spheres just touch, A' is an empirically determined parameter, E is the relative energy of the collision, and $\omega = 2/n$. Experimental data have shown that when $n = 8$ this model is a good approximation for most interactions at collision energies up to about 1 eV. That value yields $\omega = 0.25$, which is what has been used in the TRAMP and SOCRATES models up to this point. In an orbital ram burn, however collisions at relative energies up to about 5 eV are important. At 5 eV the repulsive potential softens significantly from the inverse r-to-the-nth formalism and is fit better over the extended energy range by an exponential $\exp(-r/l)$ dependence, where l is a characteristic length parameter.[29]

An interim solution to fitting the data, without requiring the coding of a more universal potential, was found by simply increasing the global value of ω. Because the A' parameters are determined from reference cross sections at thermal collision energies, besides representing softer, shallower sloped repulsive potentials, larger ω values yield smaller cross sections at hyperthermal energies. Figure 12 shows the fit obtained, using a value of 0.4 for ω. This modification appears justified because, in addition to improving the size of the plume, the fit of the more subtle shape of the contours, especially the egg shape of the innermost contour, is significantly improved.

As seen in the right-hand panel of Fig. 12, there is still a small difference in the scale of the plume. It was found that the linear dimension of the plume scaled inversely with the square of the atmospheric density. The atmospheric density was scaled by 40% for the final data/model comparisons.

Evidence for Unmixedness

An attempt to simulate what appears to be noise in the OMS high ram burn led to an interesting discovery that was consistent with the postulated source of the precursor CH_4. The small-scale fluctuations in intensity, indicated by the roughness of the contours, are not constant in magnitude across the image and are significantly larger than the statistical uncertainty (shot noise), yet they were found to have a proportionality to the local intensity. The effect of adding a fluctuation component proportional to the local intensity to the model predictions is shown in Fig. 13. A deconvolving of the modeled fluctuations from the time averaging used in producing the data image indicates that the intensity at a particular point in the plume can vary by a multiplicative factor of three. These fluctuations are taken as an indication of inhomogeneity in the precursor species CH_4 in the plume along the flow direction, yielding a temporal variation in the local, but not integrated, plume radiance. This "blotchiness" is in contrast to striations in the plume, which is the usual symptom of unmixedness.

Radiance and Radiant Intensity Comparisons

Figure 14 shows the results of the DSMC model calculation for burns identified in Tables 1 and 2 and shown in Fig. 7. Random fluctuations have been added to simulate the fluctuations seen in the data. An ω value of 0.4 was used for the ram and perpendicular burns, while the value of 0.25 from thermal data was used for the lower energy wake-biased burns. Figure 15 shows the radiant intensities from the model calculations shown in Fig. 14 compared to the measured intensities from Fig. 7. The strong dependence on angle of attack represents sensitivity to the high activation energy of reaction (2).

The intensities and spatial distribution predicted, although in reasonable agreement with the data, are likely not a unique result from the choice of the uncertain parameters. It is expected that simultaneous modification of parameters, such as the precursor mole fraction and exponential prefactor of reaction (2a), could produce indistinguishably as good a fit to both plume radiance distribution and total plume intensity. Values assigned to such parameters are, however, constrained by plausibility arguments that limit their uncertainty to a factor of about 2.

The poorest match with intensity was found for the perpendicular burns, being underpredicted by roughly a factor of five. This was attributed to the shortcomings of the inverse r-to-the-nth potential on which the VHS model is based, not being able to accommodate the broad range of collision velocities important in that geometry. By selecting an ω value that fit the highest energy collisions sampled in a ram burn, the cross sections at intermediate energies will be too small, yielding less intensity within a limited field, which might explain the underprediction.

The RCS intensities are approximately two times higher than the OMS, relative to the model predictions using identical amounts of methane. This is attributed, in part, to fuel film cooling and poorer mixing in the lower-efficiency RCS engines, indicating twice the methane production per unit propellant flow and an inverse correlation between the methane mole fraction in the exhaust and engine efficiency. Based on the attribution of the radiance to unmixedness, it is surprising that the deviation from the model for the different engines is not larger. The similarity is taken as support for

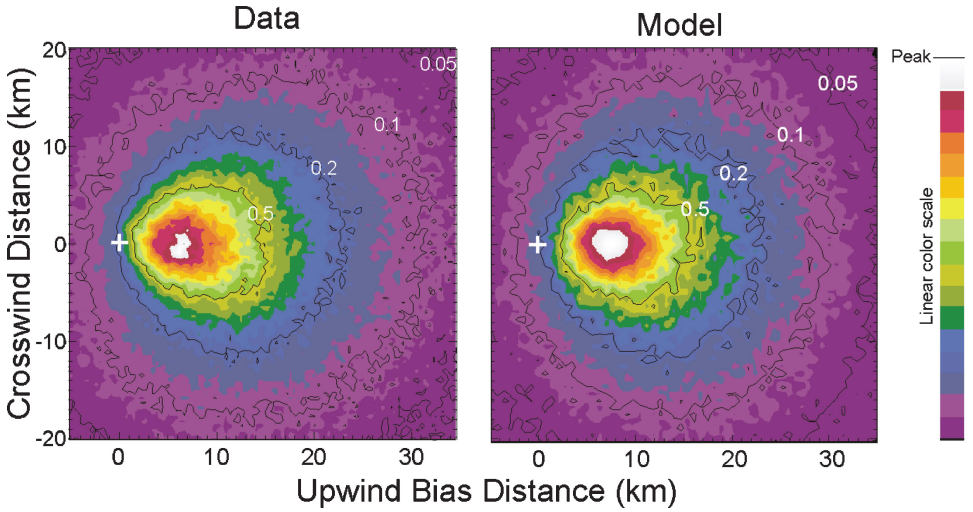

Fig. 13 Comparison of the OMS high ram burn with the model combined with a spatial fluctuation component.

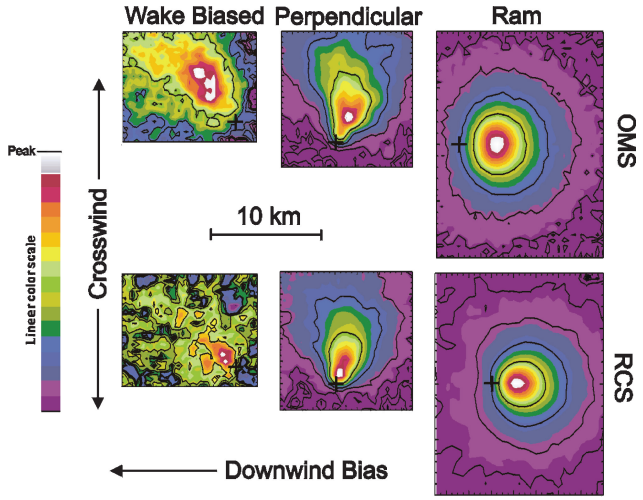

Fig. 14 DSMC model calculated burns for the scenarios represented in Fig. 7.

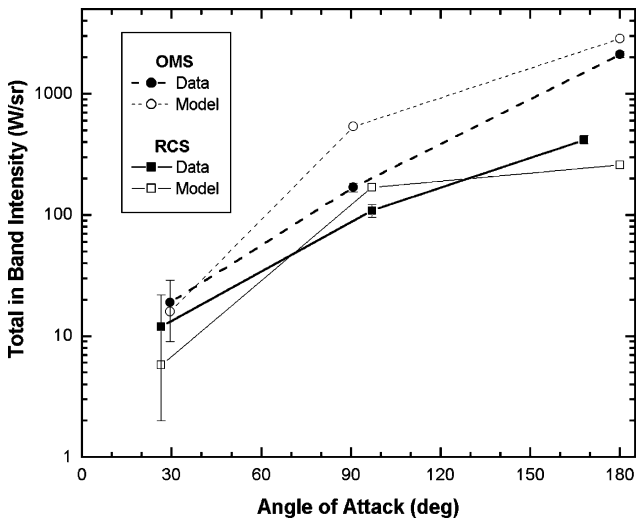

Fig. 15 Total Cameron band radiant intensities for burns shown in Fig. 7 compared to model predictions shown in Fig. 14. Computed intensities are converged to better than 1% of their value.

the existence of large variations in O/F even in engines such as the OMS, which are designed for high efficiency. Another interesting difference between the OMS and RCS engines is the contrast in the ratio of total intensity at high and low angles of attack. Although it has not been determined what is responsible for this, examining the model calculations, which show the same effect, might reveal the source.

Conclusions

The general contribution and probably most significant of this effort is the demonstration of how remote observations of radiance from low-Earth-orbit (LEO) plumes or gas releases can yield fundamental information on the chemical kinetics and dynamics of the bimolecular collision processes involved:

1) Reaction kinetics (the number of reaction steps) can be determined from the temporal dependence of total radiant intensity.

2) Total-hard-sphere scattering cross sections in a velocity range can be determined from the temporal dependence of total radiant intensity.

3) Reaction activation energy may be determined from plume morphology.

4) Reaction dynamics, such as a selected reaction proceeding through a spectator stripping mechanism vs long-lived complex, may be determinable from plume morphology.

5) Total radiance from a specific emitter is an important constraint for identifying the precursor and mechanism producing the emission.

Analysis through direct simulation Monte Carlo (DSMC) modeling can yield fundamental information about the atoms and molecules involved, comparable to carefully designed laboratory experiments.

The more specific contributions include the determination of the parameters defining the complex production of Cameron band emission by rocket engine plumes in LEO:

1) Both two- and three-step processes are involved in CO(a) formation.

2) CH_4 is a likely precursor to CO(a) formation.

3) Spectator stripping is involved in the reaction $CH_4 + O \rightarrow CH_3 + OH$.

4) The reaction $CH_3 + O \rightarrow CO(a) + H + H_2$ is a likely source of CO(a).

5) Spectator stripping in the first step and significant activation energy in the second step of the two-step process are required to fit the plume morphology.

6) CH, CH_2, and CHOH are plausible reactants with O to produce CO(a) (as the last step of the three-step mechanism).

Another specific contribution with potential direct utility is the prediction that high-altitude CO(a) radiant intensity and CH_4 mole

fraction in plumes for similar propellants is probably inversely proportional to engine efficiency.

Additional specific contributions are the implications about DSMC modeling. Molecular cross sections fit by the VHS model at thermal energies yield cross sections that are too large when extrapolated to the hyperthermal regime. An improved repulsive potential is needed to span collision energies from thermal to hyperthermal energies.

Because the mechanism determined here is relatively complex and determined through indirect observation of the attributed species, the assignment of methane as the precursor is considered tentative. The self-consistency among the predictions and observations and the difficulty with finding alternative mechanisms that produce the observed intensity and spatial distributions strongly support the assignment. A definitive verification experiment would be to release a known quantity of methane in LEO and observe the spectral radiance from Cameron band emission. Agreement between the observed radiance and the DSMC prediction should be a stringent test of the identity of the precursor and validation of the mechanism. Small differences can be used to hone the parameters defining the newly postulated chemistry and the physics of the hyperthermal interactions. Validation of the involvement of methane would also contribute to confidence in the assignment of the subsequent chemical steps postulated for the production of CO(a).

The success in extracting fundamental information in this study reflects the power of modeling. In performing this analysis, it has been found that discrepancies between the model and data represent an opportunity to gain better understanding by either adjusting the parameters of the model or improving the model. Although much was learned in the analysis reported here, the remaining discrepancies in the comparison represent the opportunity to gain still more information from the data.

Acknowledgments

Many people contributed to the success of this experiment. Only a few of those are mentioned here. A. T. Stair, of Visidyne, Inc., as Project Scientist for the Midcourse Space Experiment (MSX) program, conceived the MSX Shuttle Plume Observations (SPO) experiments. His insight that the experiments could be conducted through collaboration between NASA and the Ballistic Missile Defense Organization with the Space Test Program (STP) providing the interface led to all of the experiments reported here. The STS-85 and STS-93 mission pilots (Kent Rominger and Jeffrey Ashby) and commanders (Curt Brown and Eileen Collins) went through training and performed the burns for the SPO experiment flawlessly. The space transportation system (STS) mission INCO, Chris Counts, and coworkers provided the shuttle transmissions and antenna selections for MSX to acquire and track the orbiters, providing a critical element to the success of the experiment. The STS mission flight dynamics officers provided the critical mission dynamic analysis and state vectors required for performing and observing engine burns. MSX mission management, in particular John Mill as original MSX program manager and later as project scientist and Bruce Guilmain as MSX program manager; and mission support from Johns Hopkins University, Applied Physics Laboratory, in particular Rick Shelton, Alice Bowman, Jeff Taylor, Gene Heyler, James Carbary, and Pat McEvaddy, contributed significantly. Terry Hols, Darin Walker, Larry Dungan, Rich Martinez, Craig Lamb, Gus Hernandez, and Todd Nichols of the STP supplied the coordination between MSX and NASA. Rey Urbano and Jack Lyons at the Aerospace Corporation provided conjunction analysis around the clock, crucial to the success of the experiments. Mike Gersh of Spectral Sciences, Inc. (SSI), provided valuable input in helping to design and analyze the experiments. Edmond Murad, of the Air Force Research Laboratory, as experiment scientist, and Carl Rice, of The Aerospace Corporation, as alternate lead experimenter, helped support the experiment. Fritz Bien and Mike Matthew of SSI supported acquiring data on the STS-93 experiments. Matt Braunstein of SSI helped in using and modifying the SOCRATES code. Robert Field of Massachusetts Institute of Technology and John Cox of the Northrop Grumman Corporation provided Franck–Condon factors for the analysis of the Cameron band spectrum.

References

[1]Oakes, D. B., Sonnenfroh, D. M., and Caledonia, G. E., "Velocity Dependent O Atom IR Excitation Cross Sections: Connections with Flight Data," *Journal of Geophysical Research*, Vol. 99, No. A12, 1994, pp. 23,249–23,255.

[2]Orient, O. J., and Chutjian, A., "Observation of CH $A \rightarrow X$, CN $B \rightarrow X$, and NH $A \rightarrow X$ Emission in Gas-phase Collisions of Fast O(^{3}P) Atoms with Hydrazines," *Journal of Chemical Physics*, Vol. 101, No. 10, 1994, pp. 8297–8301.

[3]Garton, D. J., Minton, T. K., Troya, D., Pascual, R., and Schatz, G. C., "Hyperthermal Reactions of O(^{3}P) with Alkanes: Observations of Novel Reaction Pathways in Crossed-Beams and Theoretical Studies," *Journal of Physical Chemistry A*, Vol. 107, No. 23, 2003, pp. 4583–4587.

[4]Simmons, F. S., *Rocket Exhaust Plume Phenomenology*, 1st ed., The Aerospace Press, El Segundo, CA, 2000.

[5]Broadfoot, A. L., Anderson, E., Sherard, P., Knecht, D. J., Vierek, R. A., Pike, C. P., Murad, E., Elgin, J. E., Bernstein, L. S., Kofsky, I. L., Rall, D. L., Blaha, J., and Culbertson, F. L., "Spectrographic Observation at Wavelengths Near 630 nm of the Interaction Between the Atmosphere and the Space Shuttle Exhaust," *Journal of Geophysical Research*, Vol. 97, No. A12, 1992, pp. 19501–19508.

[6]Viereck, R. A., Murad, E., Knecht, D. J., and Pike, C. P., "The Interaction of the Atmosphere with the Space Shuttle Thruster Plume: the NH(A-X) 336 nm Emission," *Journal of Geophysical Research*, Vol. 101, No. A3, 1996, pp. 5371–5380.

[7]Murad, E., "The Shuttle Glow Phenomenon," *Annual Review of Physical Chemistry*, Vol. 49, Annual Reviews, Inc., Palo Alto, CA, 1998, pp. 73–98.

[8]Mill, J. D., O'Neil, R. R., Price, S., Romick, G. J., Uy, O. M., Gaposchkin, E. M., Light, G. C., Moore, W. W., Jr., Murdock, T. L., and Stair, A. T., Jr., "Midcourse Space Experiment: Introduction to the Spacecraft, Instruments and Scientific Objectives," *Journal of Spececraft and Rockets*, Vol. 31, No. 5, 1994, pp. 900–907.

[9]Carbary, J. F., Darlington, E. H., Harris, T. J., McEvaddy, P. J., Mayr, M. J., Peacock, K., and Meng, C. I., "Ultraviolet and Visible Imaging and Spectrographic Imaging Instrument," *Applied Optics*, Vol. 33, No. 19, 1994, pp. 4201–4213.

[10]Hedin, A. E., "MSIS-86 Thermospheric Model," *Journal of Geophysical Research*, Vol. 92, No. A5, 1987, pp. 4649–4662.

[11]Hedin, A. E., "Extension of the MSIS Thermosphere Model into the Middle and Lower Atmosphere," *Journal of Geophysical Research*, Vol. 96, No. A2, 1991, pp. 1159–1172.

[12]Rees, M. H., *Physics and Chemistry of Upper Atmosphere*, 1st ed., Cambridge Univ. Press, Cambridge, MA, 1989, p. 98.

[13]Slanger, T. G., and Black, G., "CO(a $^3\Pi$), Its Production, Detection, Deactivation, and Radiative Lifetime," *Journal of Chemical Physics*, Vol. 55, No. 5, 1971, pp. 2164–2173.

[14]Bernstein, L. S., Chiu, Y., Gardner, J. A., Broadfoot, A. L., Lester, M. I., Tsiouris, M., Dressler, R. A., and Murad, E., "Molecular Beams in Space: Sources of OH(A-X) Emission in the Space Shuttle Environment," *Journal of Physical Chemistry*, Vol. 107, No. 49, 2003, pp. 10,695–10,705.

[15]Nickerson, C. R., Dang, L. D., and Coats, D. E., "Two Dimensional Kinetics Reference Computing Program," Ultrasystems, Inc., NASA Contract No. NAS8-35931, April 1985.

[16]Elgin, J. B., Cooke, D. C., Tautz, M. F., and Murad, E., "Modeling of Atmospherically Induced Gas Phase Optical Contamination from Orbiting Spacecraft," *Journal of Geophysical Research*, Vol. 95, No. A8, 1990, pp. 12197–12208.

[17]Elgin, J., and Bernstein, L. S., "The Theory Behind the Socrates Code," Phillips Lab., PL-TR-92-2207, Hanscom AFB, MA, Aug. 1992.

[18]Bird, G. A., "Monte Carlo in an Engineering Context," *Rarefied Gas Dynamics*, edited by S. S. Fisher, Progress in Aeronautics and Astronautics, AIAA, New York, 1980, pp. 239–255.

[19]Caledonia, G. E., and Person, J. C., "The Interpretation of Space Shuttle Measurements of Ionic Species," *Journal of Geophysical Research*, Vol. 92, No. A1, 1987, pp. 273–281.

[20]Barth, C. A., Hord, C. W., Pearce, J. B., Kelly, K. K., Anderson, G. P., and Stewart, A. I., "Mariner 6 and 7 Ultraviolet Spectometer Experiment: Upper Atmosphere Data," *Journal of Geophysical Research*, Vol. 76, No. 10, 1971, pp. 2213–2227.

[21]Conway, R. R., "Spectroscopy of the Cameron Bands in the Mars Airglow," *Journal of Geophysical Research*, Vol. 86, No. A6, 1981. pp. 4767–4775.

[22]Skrzypkowski, M. P., Gougousi, T., Johnsen, R., and Golde, M. F., "Measurement of the Absolute Yield of CO(a $^3\Pi$) + O Products in the Dissociative Recombination of CO_2^+ Ions with Electrons," *Journal of Chemical Physics*, Vol. 108, No. 20, 1998, pp. 8400–8407.

[23]Burke, M. L., Dimpfl, W. L., Sheaffer, P. M., Zittel, P. F., and Bernstein, L. S., "Formation of Triplet CO in Atomic Oxygen Flames of Acetylene and Carbon Suboxide," *Journal of Physical Chemistry*, Vol. 100, No. 1, 1996, pp. 138–148.

[24]Mallard, W. G., Westley, F., Herron, J. T., and Hampson, R. F., NIST Chemical Kinetics Database, Ver. 6.0, NIST Standard Reference Data, National Inst. of Standards and Technology, Gaithersburg, MD, 1994.

[25]Troya, D., Pascual, R. X., and Schatz, G. C., "Theoretical Studies of the O(^{3}P) + Methane Reaction," *Journal of Physical Chemistry A*, Vol. 107, No. 49, 2003, pp. 10497–10506.

[26]Troya, D., Schatz, G. C., Garton, D. J., Brunsvold, A. L., and Minton, T., "Crossed-Beams and Theoretical Studies of the O(^{3}P) + $CH_4 \rightarrow H + OCH_3$ Reaction Excitation Function," *Journal of Chemical Physics*, Vol. 120, No. 2, 2004, pp. 731–739.

[27]Seakins, P. W., and Leone, S. R., "A Laser Flash Photolysis/Time-Resolved FTIR Emission Study of a New Channel in the Reaction of CH_3 + O: Production of CO(v)," *Journal of Physical Chemistry*, Vol. 96, No. 11, 1992, pp. 4478–4485.

[28]Levine, R. D., and Bernstein, R. B., *Molecular Reaction Dynamics and Chemical Reactivity*, 1st ed., Oxford Univ. Press, New York, 1987, p. 112.

[29]Pauly, H., "Elastic Scattering Cross Sections I: Spherical Potentials," *Atom-Molecule Collision Theory*, edited by R. B. Bernstein, Plenum, New York, 1979, pp. 111–199.

I. Boyd
Associate Editor